

Room-Temperature Activation of InGaZnO Thin-Film Transistors via He⁺ Irradiation

Michael G. Stanford,^{†,§} Joo Hyon Noh,^{†,§} Kyle Mahady,[†] Anton V. Ievlev,^{‡,§} Peter Maksymovych,[‡] Olga S. Ovchinnikova,[‡] and Philip D. Rack^{*,†,‡}

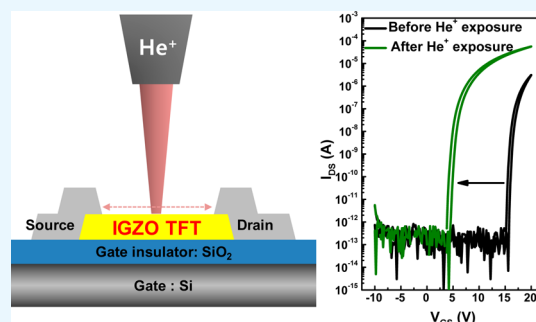
[†]Department of Materials Science and Engineering, The University of Tennessee, Knoxville, Tennessee 37996, United States

[‡]Center for Nanophase Materials Sciences, Oak Ridge National Laboratory, Oak Ridge, Tennessee 37831, United States

Supporting Information

ABSTRACT: Amorphous indium gallium zinc oxide (a-IGZO) is a transparent semiconductor which has demonstrated excellent electrical performance as thin-film transistors (TFTs). However, a high-temperature activation process is generally required which is incompatible for next-generation flexible electronic applications. In this work, He⁺ irradiation is demonstrated as an athermal activation process for a-IGZO TFTs. Controlling the He⁺ dose enables the tuning of charge density, and a dose of 1×10^{14} He⁺/cm² induces a change in charge density of 2.3×10^{12} cm⁻². Time-dependent transport measurements and time-of-flight secondary ion mass spectroscopy (ToF-SIMS) indicate that the He⁺-induced trapped charge is introduced because of preferential oxygen-vacancy generation. Scanning microwave impedance microscopy confirms that He⁺ irradiation improves the conductivity of the a-IGZO. For realization of a permanent activation, IGZO was exposed with a He⁺ dose of 5×10^{14} He⁺/cm² and then aged 24 h to allow decay of the trapped oxide charge originating for electron–hole pair generation. The resultant shift in the charge density is primarily attributed to oxygen vacancies generated by He⁺ sputtering in the near-surface region.

KEYWORDS: low-temperature activation, IGZO, flexible electronics, helium ion, transistors, athermal



INTRODUCTION

Amorphous metal oxide semiconductors (AMOSs), for instance, amorphous indium gallium zinc oxide (a-IGZO), have been intensively researched in the past decade because of their excellent electrical performance as thin-film transistors (TFTs) in addition to their low process temperature and superior uniformity over large areas.¹ These merits make AMOS a promising candidate to replace amorphous silicon (a-Si) TFTs for a number of next-generation electronic applications such as transparent flexible displays, electronic skins, or wearable electronics.^{2–10} The key requirement for the next-generation flexible electronic applications is the direct fabrication of electronic devices, especially TFTs, on flexible substrates.^{3,7} Thus, lowering the processing temperature for compatibility with cheap and flexible polymer substrate materials is essential for the future of AMOS TFTs. To this end, many efforts have been focused on the development of lowering the process temperature in solution-processed AMOS materials primarily for low-cost and large-area electronics. These include ultraviolet photochemical activation of sol–gel precursors,^{11,12} combustion chemistry of various precursors,^{12,13} sol–gel on chip,¹⁴ and spray pyrolysis,^{15,16} to name a few. However, solution-processed AMOS-based TFTs, in general, have relatively low carrier mobility and require relatively high postprocessing temperatures (typically ≥ 300

°C) to facilitate metal–oxygen network formation, densification, and impurity removal.^{17–19}

On the other hand, vacuum-deposited AMOS TFTs exhibit relatively high device performance with significantly higher carrier mobility [up to $30 \text{ cm}^2/(\text{V s})$]. The electrical properties are strongly dependent on oxygen vacancies in the AMOS channel layer. Therefore, to achieve good device performance, physical vapor-deposited AMOS TFTs typically require postdeposition thermal annealing to remove^{20,21} or to oxidize the AMOS channel layer;¹⁰ however, the requisite temperature is too high for many polymer substrates. While precise oxygen partial pressure control during AMOS deposition can make high-quality AMOS TFTs as-deposited, the process window is narrow and the electrical properties can be easily affected by other postprocessing steps, especially the device passivation process. In general, the process of high oxygen partial pressure during AMOS deposition and removal of excess oxygen by postthermal annealing is typically done. Recently, it has been demonstrated that the room-temperature field-induced activation via ionic liquid biasing of sputter-deposited a-IGZO channel layers achieved good TFT performance; excess oxygen

Received: July 17, 2017

Accepted: September 21, 2017

Published: September 21, 2017

was removed by the high electric field generated by the ionic liquid electrical double layer.²² Various ion beams have also demonstrated potential for room-temperature processing and doping of semiconductors.^{23–32} In this work, we demonstrate an athermal activation process of a-IGZO TFTs using He implantation which is compatible with next-generation flexible electronic applications. A schematic of the He⁺ irradiation process is shown in Figure 1a. A helium-ion microscope was

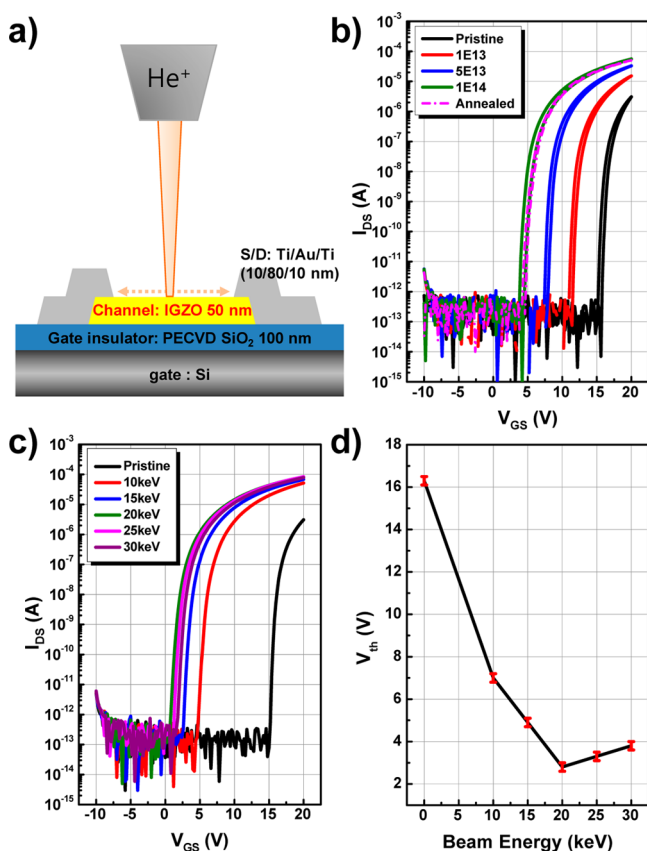


Figure 1. (a) Schematic of the a-IGZO TFT structure. A focused He⁺ beam was used to irradiate the IGZO channel. (b) Transfer curves of a-IGZO TFTs as a function of the He⁺ dose. A TFT which was activated by a postsynthesis anneal (see the Experimental Section) is shown for comparison. (c) Effects of He⁺ beam energy on the transfer curves for devices were exposed with a dose of 1×10^{14} He⁺/cm². (d) Threshold voltage (V_{th}) of the TFTs reported in part c.

used to irradiate the channel layer, with convenient control of the beam energy, dose, and selected area patterning. While silicon substrates are used to characterize the effects of He⁺ implantation parameters on the a-IGZO transport properties, the athermal IGZO activation should be compatible with low-temperature polymer substrates, and large-area ion beam processing.^{33,34}

EXPERIMENTAL SECTION

a-IGZO TFT Fabrication. An inverted staggered structure was used to fabricate a-IGZO TFTs. A heavily doped p-type Si was used for the common gate electrode (0.1–0.0 Ω cm). A 100 nm thick SiO₂ gate dielectric layer was deposited by plasma-enhanced chemical vapor deposition (PECVD), and subsequently an a-IGZO channel area was photolithographically patterned. A 50 nm thick a-IGZO layer was deposited by RF magnetron sputtering at room temperature. The rf power was 80 W, and the sputtering pressure was 5 mTorr with a 10% mixing ratio of argon and oxygen, respectively, at a fixed total flow rate

of 25 sccm. The a-IGZO active area was formed by a lift-off process. The Ti/Au/Ti (10/80/10 nm) source and drain (S/D) electrodes were deposited by e-beam evaporation and also patterned by a lift-off method. The TFT semiconductor channel width (W) and length (L) were 10 and 5 μ m, respectively. For comparison, one TFT array was annealed at 250 $^{\circ}$ C in air ambient for 1 h.

Helium-Ion Implantation. Scanning helium-ion implantation and patterning were conducted in a Zeiss ORION NanoFab helium-ion microscope which can vary the beam energy, beam current, dwell time, and pixel pitch, and is programmed to selectively pattern regions of interest. The IGZO was exposed to doses ranging from 1×10^{12} to 1×10^{15} cm⁻², in order to elucidate the dose effect on electrical transport properties. Dose was controlled by varying the number of patterning loops and current. The acceleration voltage was varied from 10 to 30 keV in order to study the effects of ion energy. Beam current for all reported exposures was 0.5 pA. For standard exposures, a constant He⁺ pixel spacing of 8 nm was used with a controlled beam defocus (50 μ m) in order to ensure uniform ion exposure in the IGZO film. Dwell time of 1 μ s per pixel was used for all exposures. A schematic diagram of the device cross section and top view for He⁺ implantation are shown in Figure 1. The He⁺-implanted area covers the entire IGZO channel area and extends ~ 1 μ m over in all directions, as shown in Figure 1.

Device Measurement. a-IGZO TFT electrical characteristics were measured using a semiconductor device analyzer (Agilent Tech B1500 A) in dark ambient. All initial measurements were performed within 2 h after He⁺ irradiation.

Microwave Characterization. To directly detect the position of the conducting regions that are created by the He⁺ exposures, we employed a near-field scanning microwave impedance microscope (sMIM) operating at a frequency $f \approx 3$ GHz. Microwave microscopy has previously been shown to be capable of detecting and characterizing conducting entities, such as ferroelectric domain walls,³⁵ 2D semiconductors,³⁶ and buried sheets of graphene.³⁷ Microwave imaging and measurements were performed in ambient with a ScanWave (Prime Nano, Inc.) sMIM add-on unit installed on an Asylum Research MFP-3D atomic force microscope. Fully shielded sMIM cantilever probes (Prime Nano, Inc.; see also ref 35) had spring constants in a range 7–8 N/m. Using built-electronics and calibration protocols, the detected microwave signal was deconvolved into two orthogonal signals, roughly proportional to the capacitance (sMIM-C) and conductance (sMIM-G) of the studied object (or imaginary and real parts of admittance, correspondingly). To correctly define the sMIM-C and sMIM-G channels, the ScanWave's detector phase was adjusted while imaging a set of 1 μ m diameter capacitors of an SMM calibration kit from MC2 Technologies. The phase was adjusted so that the variation Δ sMIM-G of the reflectometer sMIM-G signal from the capacitors was minimized; i.e., the contrast due to capacitors (assumed to be insulating) is partitioned almost entirely into the capacitive Δ sMIM-C channel. The microwave measurement probes deep into the subsurface volume of the material; therefore surface sensitivity, including surface roughness, is not a source of severe artifacts.

RESULTS AND DISCUSSIONS

Figure 1b shows the typical transfer curves of the He⁺-implanted a-IGZO TFTs as a function of He⁺ dose at a beam energy of 25 keV. For comparison, the transfer curve of an a-IGZO TFT annealed in air for 1 h at 250 $^{\circ}$ C is also included in Figure 1b. In all transfer curves, a small hysteresis (<0.6 V at 1 nA) was observed. It is clearly shown that higher dose makes a-IGZO more conductive and shifts the threshold voltage (V_{th}) to lower voltage. The He-implanted a-IGZO TFT with the dose of 1×10^{14} cm⁻² is comparable to the thermally annealed TFT at 250 $^{\circ}$ C, and therefore shows promise for low-temperature activation. The TFT parameters as a function of He⁺ dose are summarized in Table 1. The saturation field effect mobility, μ_{FE} ,

Table 1. TFT Electrical Parameters of the a-IGZO TFTs with He Implantation

device				
beam current (pA)	He dose (cm ⁻²)	V _{th} (V)	μ _{FE} [cm ² /(V s)]	SS (V/decade)
0.5	1 × 10 ¹³	12.6	8.0	0.16
	5 × 10 ¹³	9.0	8.0	0.15
	1 × 10 ¹⁴	5.6	7.9	0.18
device				
	V _{th} (V)	μ _{FE} [cm ² /(V s)]	SS (V/decade)	
250 °C annealed device	5.9	7.6	0.19	
unannealed device	16.3	6.4	0.15	

and V_{th} are calculated from a linear fitting of the forward sweep of I_{DS}^{1/2} versus V_{GS} using the saturation current equation:

$$I_{DS} = \frac{1}{2} \mu_{FE} C_i \left(\frac{W}{L} \right) (V_{GS} - V_{th})^2$$

Here, the terms are as follows: μ_{FE} is the saturation field effect mobility, W and L are the channel width and channel length, respectively, and C_i is the capacitance of the gate insulator (100 nm SiO₂).

The mobility was increased from 6.4 (unannealed TFT) to ~8 cm²/(V s) for all doses, and the subthreshold swing (SS) was <0.18 V/decade, which was comparable to that of the as-deposited TFT (0.15 V/decade). Table 2 reports the charge density that was introduced by He⁺ irradiation at the studied doses in comparison to a thermally annealed device. As mentioned, a dose of 1 × 10¹⁴ He⁺/cm² induces a similar charge density to a thermally annealed device.

Figure 1c shows the effect that He⁺ energy has on the activation of IGZO TFTs, where all devices were exposed to a dose of 1 × 10¹⁴ He⁺/cm². Changing the beam energy affects ion–solid interactions of the He⁺ with the IGZO. The studied beam energies all succeeded in shifting the V_{th} of the TFTs, however the extent varies with beam energy. Figure 1d plots ΔV_{th} as a function of beam energy. A He⁺ beam energy of 20 keV causes the largest shift in V_{th} which is optimal for IGZO activation.

For an understanding of the charge-density effect that He⁺ irradiation of varying energy has on IGZO, Stopping and Range of Ions in Matter (SRIM) Monte Carlo simulations were conducted. The Monte Carlo method has been well-documented³⁸ and can be used to estimate the range of the energetic ions in the IGZO, the sputter yield, and the energy loss of the ion, among other properties. In general, when energetic He⁺ is used to irradiate a material, the He⁺ interacts with the material via electronic and nuclear collisions. If a nuclear collision transfers a sufficient amount of energy from the ion to the target atom, the target atom can become displaced (recoil atom), creating a vacancy and interstitial. The ions and recoil atoms will generate cascading collisions in the

material, until the energy of the cascading atoms and ion is no longer sufficient to displace atomic species. Electronic energy loss during the cascading collision results in the formation of secondary electrons and electron–hole pairs. Figure 2a reports the total energy loss (electronic and nuclear) as a function of depth into the device/substrate. For all studied beam energies, the He⁺ ions penetrate through the IGZO, and energy loss occurs in the underlying SiO₂ and Si as well. As expected, ions with greater energy experience a higher amount of energy loss at all depths in the device. Energy loss in the IGZO and SiO₂ results in the formation of radiation-induced trapped charge (TC) which arises from ion implantation, generated electron–hole pairs, and structural defects in the material.³⁹ Mechanistically, the high energy He⁺ and recoil atoms generate secondary electrons via electronic energy loss during the cascading events. The ions, recoil atoms, and secondary electrons can ionize atoms within the material thus generating electron–hole (e–h) pairs. Figures S3 and S4 in the Supporting Information report Monte Carlo simulations of the deposited energy and the concentration of secondary electrons (SEs), respectively, which are generated within the IGZO and underlying SiO₂ during He⁺ exposure. Most of the deposited energy from the cascading events is in the form of electronic energy loss, and the SEs are generated with concentrations as high as 3.0 e⁻/nm³ (for an exposure dose of 1 × 10¹⁵ He⁺/cm²). This significantly contributes to the generation of e–h pairs within the IGZO and SiO₂. As the e–h pairs are generated, some will recombine. However, the free electrons can rapidly drift to ground during the He⁺ exposure because of their relatively large mean free path (ground is the gate electrode for our experimental setup during irradiation). The holes, which have a much smaller mean free path, will hop through localized states in the oxide, and some will become trapped and form a positive oxide-trap charge. Additionally, some interface-trap charges can occur.

Trapped charge in the IGZO and underlying SiO₂ can account for a shift in V_{th}. Compositional change in the IGZO stoichiometry can also result in alteration of the electronic behavior. During the thermal anneal process, which is typically used to shift V_{th} of the TFTs and hence activate the device, oxygen content is reduced where oxygen vacancies behave as n-type dopants in IGZO. Figure 2b reports the preferential sputter yield of O (γ_O) as a function of He⁺ dose, defined as [γ_O - (γ_{In} + γ_{Ga} + γ_{Zn})]. The relatively low O mass and surface binding energy is favorable for a higher sputter yield in comparison to all cation species. Preferential γ_O sputter yield decreases with increasing He⁺ energy. N-type dopants induced from preferential O sputtering can be estimated by the following equation:

$$\Delta Q = [\gamma_O - (\gamma_{In} + \gamma_{Ga} + \gamma_{Zn})] \times D \quad (1)$$

Table 2. Carrier Number Change According to the He⁺ Implantation

device					
beam current (pA)	He dose (cm ⁻²)	ΔV _{th} (V) (V _{th,unannealed} - V _{th})	ΔQ = C _i ΔV _{th} (C/cm ²)	Δcharge density (cm ⁻²)	Δcharge density in 50 nm IGZO (cm ⁻³)
0.5	1 × 10 ¹³	3.7	1.28 × 10 ⁻⁷	7.97 × 10 ¹¹	1.59 × 10 ¹⁷
	5 × 10 ¹³	7.3	2.52 × 10 ⁻⁷	1.57 × 10 ¹²	3.14 × 10 ¹⁷
	1 × 10 ¹⁴	10.7	3.69 × 10 ⁻⁷	2.30 × 10 ¹²	4.61 × 10 ¹⁷
device					
	ΔV _{th} (V) (V _{th,unannealed} - V _{th})	ΔQ = C _i ΔV _{th} (C/cm ²)	Δcharge density (cm ⁻²)	Δcharge density in 50 nm IGZO (cm ⁻³)	
250 °C annealed device	10.4	3.59 × 10 ⁻⁷	2.24 × 10 ¹²	4.49 × 10 ¹⁷	

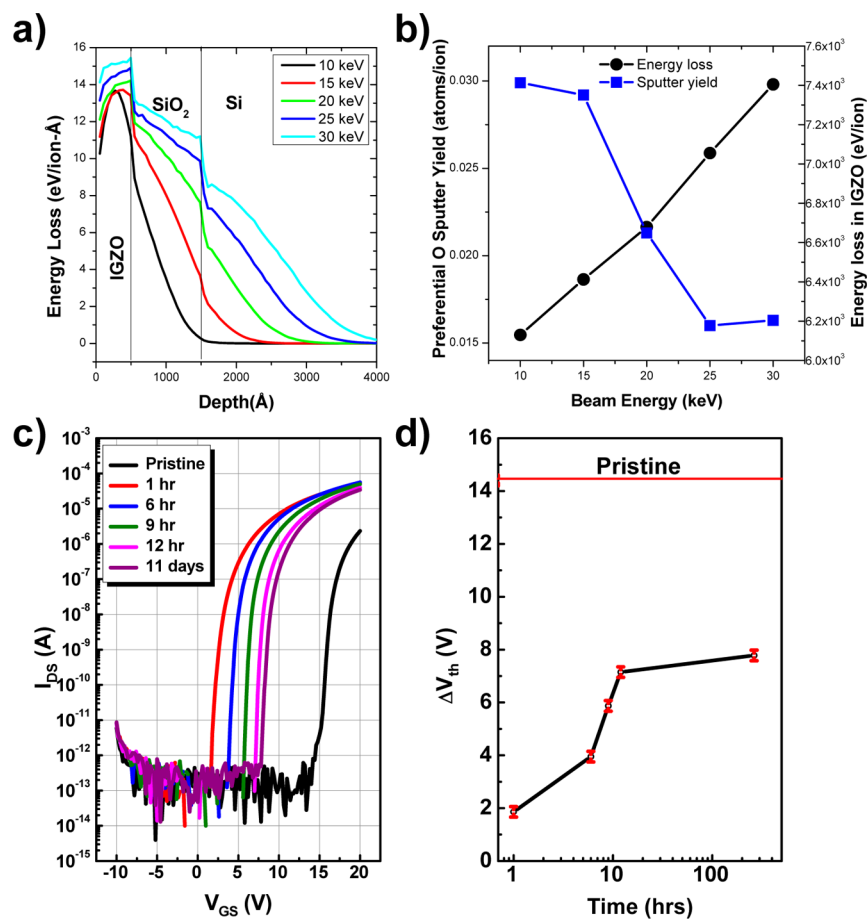


Figure 2. (a) Simulated energy loss of 10–30 keV He⁺ in the IGZO and underlying substrate calculated from Monte Carlo simulations. (b) Plot of the integrated total energy loss in the IGZO as a function of beam energy (blue, left axis). Plot of the preferential sputter yield of oxygen in comparison to those of the other metal atoms (black, right axis). Preferential sputter yield is defined by the sputter yield of oxygen minus the sputter yield of all metal atoms. (c) Time-dependent transfer curves of a device exposed with 25 keV He⁺ at a dose of 1×10^{14} He⁺/cm². (d) Threshold voltages of the TFTs in part c.

Here, the terms are as follows: ΔQ is the charge density (cm⁻²), γ is the sputter yields, and D is the He⁺ irradiation dose. From this equation, ΔQ induced by a 1×10^{14} He⁺/cm² exposure at 25 keV is approximately 1.6×10^{12} cm⁻². This theoretical value for change in charge density induced by O vacancies is in good agreement with the experimental value of 2.3×10^{12} cm⁻² which was calculated from the transfer curves and reported in Table 2.

Total energy loss (including electronic and nuclear components) of the ions in the IGZO layer is also overlaid in Figure 2b (blue). Interestingly, a simultaneous moderate γ_{O} and total energy loss occurs at an energy range approximately 18–22 keV, which resulted in the largest shift in V_{th} (Figure 1d). This suggests that trapped charge from both electron–hole generation and preferential O sputtering contributes toward the shift in V_{th} , and likely accounts for the discrepancy in ΔQ calculated by eq 1.

Trapped charge induced by electron–hole (e–h) generation is susceptible to time decay as well as bias decay.^{39,40} For verification of the contribution of e–h generation, time-dependent transfer curve measurements were conducted. Figure 2c shows the temporal evolution of the transfer curve after 25 keV He⁺ irradiation at a dose of 1×10^{14} cm⁻². For clarity, only forward sweeps are plotted. As shown in Figure 2d, the threshold voltage shifts positively with elapsed time where

the initial shift is fast and eventually saturates at a value still shifted relative to the as-deposited device. The likely explanation for the temporal V_{th} shift is positive trapped charge due to holes trapped in the oxides and secondary electron emission (positive charging).³⁹ As the trapped holes and charging decay over time, V_{th} shifts back to more positive values, but still maintains a permanent shift in V_{th} relative to a pristine device. The extent of trapped charge and atomic mixing from cascading collisions at the semiconductor/insulator interface is unclear. Monte Carlo simulations (reported in the Supporting Information, Figure S1) indicate some atomic mixing of the semiconductor and insulator. However, we expect that the effects of atomic mixing on the electronic transport are relatively small in amorphous IGZO relative to those in crystalline semiconductors. The light mass of the He⁺ generates smaller concentrations of displaced atoms compared to more massive ions because the electronic stopping power is greater than the nuclear stopping power over most of the energy range until ~ 1 keV. This will minimize atomic mixing at the interface relative to other heavier ion-target systems.

For investigation of the compositional change of the a-IGZO after He⁺ irradiation, time-of-flight secondary ion mass spectrometry (ToF-SIMS) was performed. For direct comparison, 4 different doses of He⁺ were irradiated on the same a-IGZO channel layer. Figure 3a shows ToF-SIMS scanned

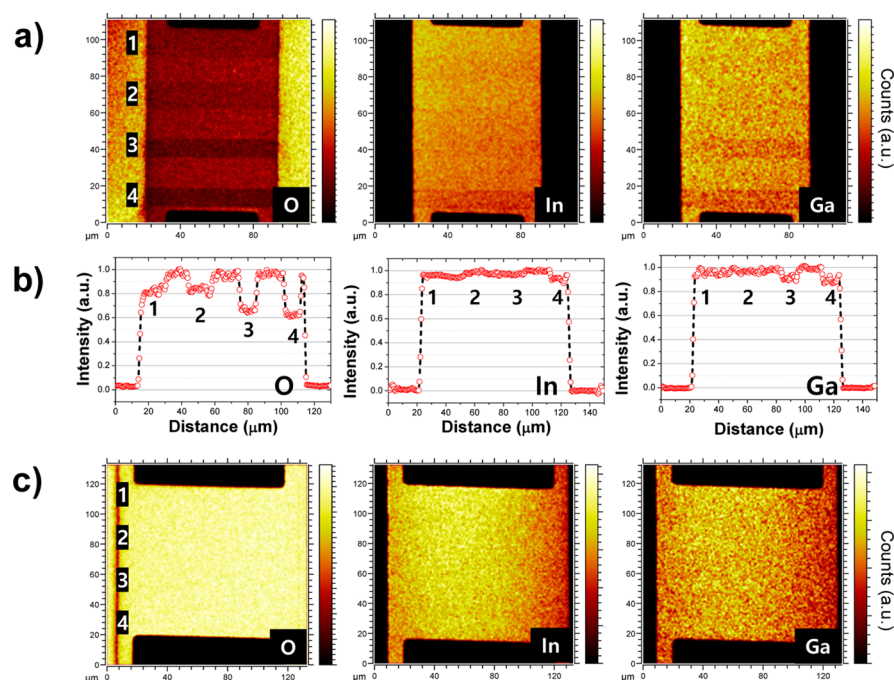


Figure 3. Time-of-flight secondary ion mass spectrometry (ToF-SIMS) map of IGZO device showing (a) O, In, and Ga species in the near-surface region after being exposed by varying He^+ doses (inset). Areas exposed with the He^+ dose are labeled from 1 to 4, which corresponds to doses 5×10^{13} , 1×10^{14} , 5×10^{14} , and 1×10^{15} He^+/cm^2 , respectively. (b) Line scan of the counts of O, In, and Ga species from top to bottom across the IGZO. (c) ToF-SIMS maps of the IGZO device at a depth of approximately 40 nm into the material.

images for the In, Ga, and O species (Zn could not be measured because of low ionization efficiency). Before measurement, the sample was sputtered by Cs ions at 1 keV to remove surface contamination. At the He^+ -irradiated areas, oxygen content was decreased, which suggests oxygen sputtering, resulting in charge-carrier generation. For the dose of 5×10^{13} and 1×10^{14} cm^{-2} , oxygen content change is clearly distinguished, but In and Ga content changes are not clearly distinguished. At higher doses ($\geq 5.0 \times 10^{14}$ He^+/cm^2), all species inexplicably appear depleted. This phenomenon is likely a charging artifact resulting from the original He^+ irradiation; therefore relative shifts in the ToF-SIMS counts should be used to estimate postirradiation stoichiometry. Figure 3b shows the O, In, and Ga content profiles along the channel length direction. It is clearly shown that low mass O was preferentially sputtered with the He^+ in comparison to In, Ga, and presumably Zn (which is predicted to have a comparable sputter yield according to Monte Carlo simulations). For investigation of the thickness of the He^+ sputtering effect, ToF-SIMS depth profiles were measured. Figure 3c shows ToF-SIMS scanned images for the In, Ga, and O species after 1 min sputtering. The estimated etched IGZO thickness is ~ 40 nm. On the IGZO channel layer, the metal and oxygen concentration gradients could not be observed, which suggests that the compositional changes upon He implantation are localized in a thin top layer (estimated around 5–15 nm). The near-surface compositional change occurs because the energetic He^+ sputters the atomic species. Although energy loss and cascading collisions continue to occur much deeper (≥ 40 nm) in the IGZO layer as well as the underlying substrate, few cations or anions are sputtered from this deep because of the short target atom/ion mean free path. Therefore, the composition changes are exhibited in the near-surface region. From the SIMS analysis, we concluded that the permanent V_{th}

shift at high He^+ dose is due to the oxygen-vacancy formation in the near-surface a-IGZO region.

For a complement to the SIMS data, scanning microwave impedance microscopy (sMIM) measurements were taken on a single channel in operando that was exposed to He^+ doses ranging from 5×10^{13} to 1×10^{15} He^+/cm^2 . Figure 4 shows the results of SMIM imaging of the device structure, with various degrees of He-ion exposure between electrodes. Three results are immediately clear: (1) There is a strong microwave

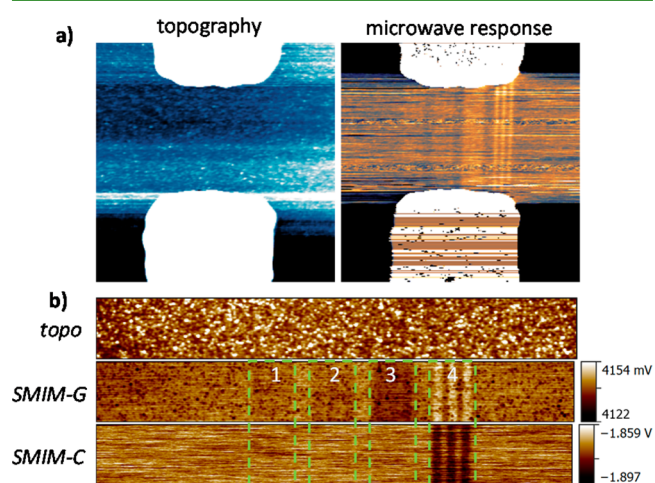


Figure 4. Microwave characterization of IGZO transistors after He irradiation. (a) Large-scale images of topography (left) and microwave response (right) of the channel region. The irradiated lines clearly show up. (b) Zoom-in onto the irradiated regions, showing both SMIM-G and SMIM-C signals in the windows of decreasing the He dose from 1 to 4, which corresponds to doses 5×10^{13} , 1×10^{14} , 5×10^{14} , and 1×10^{15} He^+/cm^2 , respectively.

signature of the He irradiation, including the contrast due to distinct localized lines for a fixed He dose (Figure 4b, M1). (2) Microwave contrast notably fades with decreasing exposure dose (Figure 4b). (3) The contrast is predominantly in the SMIM-G channel, indicating local changes in conductivity, which is consistent with the macroscopic measurements. The SMIM-C signal shows little contrast (Figure 4b), except for the largest He⁺ dose. Although crosstalk due to incomplete separation of the imaginary and real parts of the microwave response cannot be ruled out, we suggest that capacitive properties signal chemical changes in the IGZO indicative of preferential O sputtering, which appear or become detectable at higher dose.

To realize a permanent shift in V_{th} for the IGZO devices, oxygen vacancies in the IGZO must be generated since the V_{th} shift generated by e–h generation decays over time. Figure 5

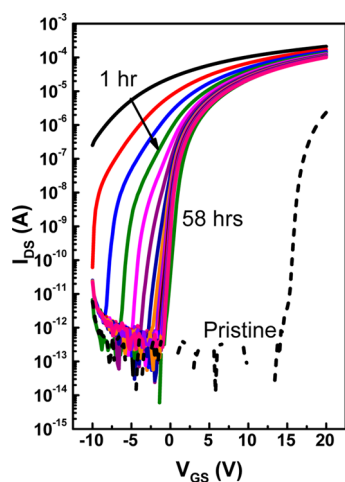


Figure 5. Transfer curves for the IGZO TFT device which was exposed with a dose of 5×10^{14} He⁺/cm². Measurements were collected in 3 h increments. A pristine untreated device is reported for comparison (---).

shows a transfer curve of an IGZO TFT which was irradiated with a dose of 5×10^{14} He⁺/cm². Immediately after exposure, large shifts in V_{th} resulted in metallic behavior over the V_{GS} range studied. The device was then allowed to age for 58 h to allow the e–h generated trapped charge to decay. After aging for >24 h, the device demonstrated more ideal characteristics of an “activated” device. A dose of 5×10^{14} He⁺/cm² resulted in a V_{th} of ~ -1 V. From ΔV_{th} , it is estimated that the charge density, presumably introduced by O-vacancy creation, is 3.1×10^{12} cm⁻². Therefore, the exposure and aging strategy can be used to induce a permanent shift in V_{th} and provide a method for low-temperature activation. In addition, positive bias, negative bias, and light-illuminated negative bias stress tests were performed on He⁺-activated samples (see the Supporting Information, Figures S5 and S6 for details).

CONCLUSIONS

In conclusion, athermal a-IGZO TFT activation is demonstrated using He⁺ irradiation. The mechanism of the He⁺-irradiation effects on the a-IGZO TFT parameters is modeled as radiation-induced trapped charge due to e–h generation and oxygen-vacancy formation. The larger V_{th} shift with the higher dose is demonstrated, and partial V_{th} recovery with the elapse of time after He⁺ implantation is observed, which is attributed to

the dissipation of the trapped charge in the gate insulator. Although the TFTs with low dose ($<1 \times 10^{13}$ cm⁻²) are recovered to the original state, the TFTs with high dose showed permanent negative V_{th} shift which is attributed to the oxygen-vacancy formation in the near-surface region of the a-IGZO layer.

ASSOCIATED CONTENT

Supporting Information

The Supporting Information is available free of charge on the ACS Publications website at DOI: 10.1021/acsami.7b10449.

Description of Monte Carlo simulations and bias stress tests; additional figures of cross sections, trajectories, energy-loss densities, and stability test results (PDF)

AUTHOR INFORMATION

Corresponding Author

*E-mail: prack@utk.edu.

ORCID

Michael G. Stanford: 0000-0001-9663-1138

Anton V. Ievlev: 0000-0003-3645-0508

Author Contributions

[§]M.G.S. and J.H.N. are co-first authors.

Funding

This manuscript has been authored by UT-Battelle, LLC, under Contract DE-AC05-00OR22725 with the U.S. Department of Energy. The United States Government retains and the publisher, by accepting the article for publication, acknowledges that the United States Government retains a nonexclusive, paid-up, irrevocable, worldwide license to publish or reproduce the published form of this manuscript, or allow others to do so, for United States Government purposes. The Department of Energy will provide public access to these results of federally sponsored research in accordance with the DOE Public Access Plan (<http://energy.gov/downloads/doe-public-access-plan>).

Notes

The authors declare no competing financial interest.

ACKNOWLEDGMENTS

P.D.R. and J.H.N. acknowledge support from the National Science Foundation under Grant CNS 1544686. M.G.S. acknowledges support from the US Department of Energy (DOE) under Grant DOE DE-SC0002136. P.D.R., O.S.O., A.V.I., J.H.N., and M.G.S. acknowledge that the IGZO transistor fabrication, helium-ion microscope exposures, ToF-SIMS, and scanning microwave microscopy was conducted at the Center for Nanophase Materials Sciences, which is a DOE Office of Science User Facility under user proposal CNMS2016-216.

REFERENCES

- Nomura, K.; Ohta, H.; Takagi, A.; Kamiya, T.; Hirano, M.; Hosono, H. Room-Temperature Fabrication of Transparent Flexible Thin-Film Transistors Using Amorphous Oxide Semiconductors. *Nature* **2004**, *432* (7016), 488–492.
- Adamopoulos, G.; Thomas, S.; Wöbkenberg, P. H.; Bradley, D. D. C.; McLachlan, M. A.; Anthopoulos, T. D. High-Mobility Low-Voltage ZnO and Li-Doped ZnO Transistors Based on ZrO₂ High-K Dielectric Grown by Spray Pyrolysis in Ambient Air. *Adv. Mater.* **2011**, *23* (16), 1894–1898.

- (3) Cherenack, K.; Zysset, C.; Kinkeldei, T.; Münzenrieder, N.; Tröster, G. Woven Electronic Fibers with Sensing and Display Functions for Smart Textiles. *Adv. Mater.* **2010**, *22* (45), 5178–5182.
- (4) Fortunato, E.; Barquinha, P.; Martins, R. Oxide Semiconductor Thin-Film Transistors: A Review of Recent Advances. *Adv. Mater.* **2012**, *24* (22), 2945–2986.
- (5) Ito, M.; Kon, M.; Miyazaki, C.; Ikeda, N.; Ishizaki, M.; Matsubara, R.; Ugajin, Y.; Sekine, N. Amorphous Oxide TFT and Their Applications in Electrophoretic Displays. *Phys. Status Solidi A* **2008**, *205* (8), 1885–1894.
- (6) Lee, K.-H.; Kim, S.-M.; Jeong, H.; Pak, Y.; Song, H.; Park, J.; Lim, K.-H.; Kim, J.-H.; Kim, Y. S.; Ko, H. C.; Kwon, I. K.; Jung, G.-Y. All-Solution-Processed Transparent Thin Film Transistor and Its Application to Liquid Crystals Driving. *Adv. Mater.* **2013**, *25* (23), 3209–3214.
- (7) Münzenrieder, N.; Zysset, C.; Petti, L.; Kinkeldei, T.; Salvatore, G. A.; Tröster, G. Flexible Double Gate a-IGZO TFT Fabricated on Free Standing Polyimide Foil. *Solid-State Electron.* **2013**, *84*, 198–204.
- (8) Salvatore, G. A.; Münzenrieder, N.; Kinkeldei, T.; Petti, L.; Zysset, C.; Strelbel, I.; Büthe, L.; Tröster, G. Wafer-Scale Design of Lightweight and Transparent Electronics That Wraps around Hairs. *Nat. Commun.* **2014**, *5*, 2814–2821.
- (9) Tomchenko, A. A.; Harmer, G. P.; Marquis, B. T.; Allen, J. W. Semiconducting Metal Oxide Sensor Array for the Selective Detection of Combustion Gases. *Sens. Actuators, B* **2003**, *93* (1), 126–134.
- (10) Kim, W.-G.; Tak, Y. J.; Du Ahn, B.; Jung, T. S.; Chung, K.-B.; Kim, H. J. High-Pressure Gas Activation for Amorphous Indium-Gallium-Zinc-Oxide Thin-Film Transistors at 100 °C. *Sci. Rep.* **2016**, *6*, 23039.
- (11) Kim, Y.-H.; Heo, J.-S.; Kim, T.-H.; Park, S.; Yoon, M.-H.; Kim, J.; Oh, M. S.; Yi, G.-R.; Noh, Y.-Y.; Park, S. K. Flexible Metal-Oxide Devices Made by Room-Temperature Photochemical Activation of Sol-gel Films. *Nature* **2012**, *489*, 128–132.
- (12) Park, S.; Kim, K.-H.; Jo, J.-W.; Sung, S.; Kim, K.-T.; Lee, W.-J.; Kim, J.; Kim, H. J.; Yi, G.-R.; Kim, Y.-H.; Yoon, M.-H.; Park, S. K. In-Depth Studies on Rapid Photochemical Activation of Various Sol-Gel Metal Oxide Films for Flexible Transparent Electronics. *Adv. Funct. Mater.* **2015**, *25* (19), 2807–2815.
- (13) Kim, M.-G.; Kanatzidis, M. G.; Facchetti, A.; Marks, T. J. Low-Temperature Fabrication of High-Performance Metal Oxide Thin-Film Electronics via Combustion Processing. *Nat. Mater.* **2011**, *10*, 382–388.
- (14) Banger, K. K.; Yamashita, Y.; Mori, K.; Peterson, R. L.; Leedham, T.; Rickard, J.; Sirringhaus, H. Low-Temperature, High-Performance Solution-Processed Metal Oxide Thin-Film Transistors Formed by a sol-Gel on Chip Process. *Nat. Mater.* **2011**, *10*, 45–50.
- (15) Bashir, A.; Wöbkenberg, P. H.; Smith, J.; Ball, J. M.; Adamopoulos, G.; Bradley, D. D. C.; Anthopoulos, T. D. High-Performance Zinc Oxide Transistors and Circuits Fabricated by Spray Pyrolysis in Ambient Atmosphere. *Adv. Mater.* **2009**, *21* (21), 2226–2231.
- (16) Faber, H.; Lin, Y.-H.; Thomas, S. R.; Zhao, K.; Pliatsikas, N.; McLachlan, M. A.; Amassian, A.; Patsalas, P. A.; Anthopoulos, T. D. Indium Oxide Thin-Film Transistors Processed at Low Temperature via Ultrasonic Spray Pyrolysis. *ACS Appl. Mater. Interfaces* **2015**, *7* (1), 782–790.
- (17) Liu, G.; Liu, A.; Zhu, H.; Shin, B.; Fortunato, E.; Martins, R.; Wang, Y.; Shan, F. Low-Temperature, Nontoxic Water-Induced Metal-Oxide Thin Films and Their Application in Thin-Film Transistors. *Adv. Funct. Mater.* **2015**, *25* (17), 2564–2572.
- (18) Socrates, J.; Banger, K. K.; Vaynzof, Y.; Sadhanala, A.; Brown, A. D.; Sepe, A.; Steiner, U.; Sirringhaus, H. Electronic Structure of Low-Temperature Solution-Processed Amorphous Metal Oxide Semiconductors for Thin-Film Transistor Applications. *Adv. Funct. Mater.* **2015**, *25* (12), 1873–1885.
- (19) Song, K.; Noh, J.; Jun, T.; Jung, Y.; Kang, H.-Y.; Moon, J. Fully Flexible Solution-Deposited ZnO Thin-Film Transistors. *Adv. Mater.* **2010**, *22* (38), 4308–4312.
- (20) Fortunato, E. M. C.; Pereira, L. M. N.; Barquinha, P. M. C.; Botelho do Rego, A. M.; Gonçalves, G.; Vilà, A.; Morante, J. R.; Martins, R. F. P. High Mobility Indium Free Amorphous Oxide Thin Film Transistors. *Appl. Phys. Lett.* **2008**, *92* (22), 222103.
- (21) Ide, K.; Kikuchi, Y.; Nomura, K.; Kimura, M.; Kamiya, T.; Hosono, H. Effects of Excess Oxygen on Operation Characteristics of Amorphous In-Ga-Zn-O Thin-Film Transistors. *Appl. Phys. Lett.* **2011**, *99* (9), 93507.
- (22) Pudasaini, P. R.; Noh, J. H.; Wong, A. T.; Ovchinnikova, O. S.; Haglund, A. V.; Dai, S.; Ward, T. Z.; Mandrus, D.; Rack, P. D. Ionic Liquid Activation of Amorphous Metal-Oxide Semiconductors for Flexible Transparent Electronic Devices. *Adv. Funct. Mater.* **2016**, *26* (17), 2820–2825.
- (23) FUNABIKI, F.; KAMIYA, T.; HOSONO, H. Doping Effects in Amorphous Oxides. *J. Ceram. Soc. Jpn.* **2012**, *120* (1407), 447–457.
- (24) Ufert, K.-D. Doping of VO₂ Thin Films by Ion Implantation. *Phys. Status Solidi* **1977**, *42* (1), 187–190.
- (25) Hosono, H.; Kikuchi, N.; Ueda, N.; Kawazoe, H.; Shimidzu, K. Amorphous Transparent Electroconductor 2CdO GeO₂: Conversion of Amorphous Insulating Cadmium Germanate by Ion Implantation. *Appl. Phys. Lett.* **1995**, *67* (18), 2663–2665.
- (26) Hosono, H.; Miyakawa, M.; Kawazoe, H.; Shimizu, K. Formation of Electronic Conducting Amorphous WO₃ Thin Films by Ion Implantation. *J. Non-Cryst. Solids* **1998**, *241* (2), 190–194.
- (27) Miyakawa, M.; Kawamura, K.; Hosono, H.; Kawazoe, H. Large Electrical Conductivity Enhancement of WO₃ Thin Films Produced by Ion Implantation. *J. Appl. Phys.* **1998**, *84*, 5610.
- (28) Narushima, S.; Hosono, H.; Jisun, J.; Yoko, T.; Shimakawa, K. Electronic Transport and Optical Properties of Proton-Implanted Amorphous 2CdO-GeO₂ Films. *J. Non-Cryst. Solids* **2000**, *274* (1), 313–318.
- (29) Sivakumar, R.; Sanjeeviraja, C.; Jayachandran, M.; Gopalakrishnan, R.; Sarangi, S. N.; Paramanik, D.; Som, T. Modification of WO₃ Thin Films by MeV N⁺-Ion Beam Irradiation. *J. Phys.: Condens. Matter* **2007**, *19* (18), 186204.
- (30) Kamiya, T.; Nomura, K.; Hosono, H. Origins of High Mobility and Low Operation Voltage of Amorphous Oxide TFTs: Electronic Structure, Electron Transport, Defects and Doping. *J. Disp. Technol.* **2009**, *5* (7), 273–288.
- (31) Chen, R.; Zhou, W.; Zhang, M.; Wong, M.; Kwok, H. S. Self-Aligned Indium-Gallium-Zinc Oxide Thin-Film Transistor With Source/Drain Regions Doped by Implanted Arsenic. *IEEE Electron Device Lett.* **2013**, *34* (1), 60–62.
- (32) Qian, L. X.; Tang, W. M.; Lai, P. T. Improved Characteristics of InGaZnO Thin-Film Transistor by Using Fluorine Implant. *ECS Solid State Lett.* **2014**, *3* (8), P87–P90.
- (33) Pearton, S. J. Ion Implantation in III-V Semiconductor Technology. *Int. J. Mod. Phys. B* **1993**, *7* (28), 4687–4761.
- (34) Das, S. K.; Kaminsky, M. Radiation Blistering of Polycrystalline Niobium by Helium-ion Implantation. *J. Appl. Phys.* **1973**, *44* (1), 25–31.
- (35) Tselev, A.; Yu, P.; Cao, Y.; Dedon, L. R.; Martin, L. W.; Kalinin, S. V.; Maksymovych, P. Microwave A.c. Conductivity of Domain Walls in Ferroelectric Thin Films. *Nat. Commun.* **2016**, *7*, 11630.
- (36) Wu, D.; Li, X.; Luan, L.; Wu, X.; Li, W.; Yogeesh, M. N.; Ghosh, R.; Chu, Z.; Akinwande, D.; Niu, Q.; Lai, K. Uncovering Edge States and Electrical Inhomogeneity in MoS₂ Field-Effect Transistors. *Proc. Natl. Acad. Sci. U. S. A.* **2016**, *113* (31), 8583–8588.
- (37) Tselev, A.; Lavrik, N. V.; Vlasiouk, I.; Briggs, D. P.; Rutgers, M.; Proksch, R.; Kalinin, S. V. Near-Field Microwave Scanning Probe Imaging of Conductivity Inhomogeneities in CVD Graphene. *Nanotechnology* **2012**, *23* (38), 385706.
- (38) Ziegler, J. F.; Ziegler, M. D.; Biersack, J. P. SRIM – The Stopping and Range of Ions in Matter (2010). *Nucl. Instrum. Methods Phys. Res., Sect. B* **2010**, *268* (11), 1818–1823.
- (39) Schwank, J. R.; Shaneyfelt, M. R.; Fleetwood, D. M.; Felix, J. A.; Dodd, P. E.; Paillet, P.; Ferlet-Cavrois, V. Radiation Effects in MOS Oxides. *IEEE Trans. Nucl. Sci.* **2008**, *55* (4), 1833–1853.

(40) Fleetwood, D. M.; Winokur, P. S.; Schwank, J. R. Using Laboratory X-Ray and Cobalt-60 Irradiations to Predict CMOS Device Response in Strategic and Space Environments. *IEEE Trans. Nucl. Sci.* **1988**, *35* (6), 1497–1505.